Atomic Force Microscope: Modeling, Simulations, and Experiments

Osamah M. El Rifai, and Kamal Youcef-Toumi

Abstract— The quality of atomic force microscope (AFM) data strongly depends on scan and controller parameters. Data artifacts can result from poor dynamic response of the instrument. In order to achieve reliable data, dynamic interactions between AFM components need to be well understood and controlled. In this paper we present a summary of our work in this direction. It includes models for the probe-sample interaction, scanner lateral and longitudinal dynamics, scanner creep, and cantilever dynamics. The models were used to study the effect of scan parameters on the system dynamics. Simulation results for both frequency response and imaging were presented. Experimental results were given supporting the simulations and demonstrating the competence of the models. The results within will be used to develop algorithms that allow automated choice of key system parameters, guaranteeing reliable and artifact-free data for any given operating condition (sample, cantilever, environment). Consequently, expanding the AFM capabilities and permitting its use in a wider range of applications.

Keywords— AFM, model, experiments, simulation, control

I. Introduction

The invention of scanning probe microscopy (SPM), and AFM in particular, has greatly contributed to advancing research in nano-science and technology to its current state of the art. The success of AFM as a tool in nano-sciences, lies in its ability to provide controlled nano-level force or displacement. Examples include nano-scale studies of plastic deformation, microstructures, and friction [1]. Other applications require surface topography information of a sample, e.g. micro-fabrication, and nano-defects.

Poor dynamic interactions between AFM components can result in corrupting AFM data, [2], and producing data artifacts. In order to achieve the best possible performance one needs to understand these dynamic interactions. In this scope, there has been some work in the literature on developing models that describe the dynamics of an AFM cantilever during intermittent-mode operation, [3]. These models focus on probe-sample interaction at a single location on the sample surface. Due to the low scanning speeds of this mode, these models do not account for the effect of scanning speed nor scanner dynamics. Therefore, these models fail to capture the overall dynamics and are not suitable for analyzing contact-mode operation, where scan speed, scanner dynamics, friction, and control system all need to be considered.

This paper presents a summary of research effort toward addressing these challenges in AFM technology. In section II, some background on AFM is given. Section III, elaborates on the motivation for this work. Models for probe-sample interactions, scanner lateral and longitudinal dynamics, scanner creep, and cantilever dynamics are presented in section IV. Sources of noise and disturbances are also discussed. Both experimental and simulation results are presented and discussed in section V. Summary and concluding remarks are given in section VI.

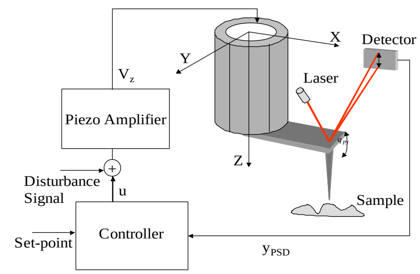

Fig. 1. Schematic diagram of AFM main components.

II. Atomic Force Microscope

An AFM, Fig. 1, has three main components, namely, a scanner, a cantilever with a sharp probe, and a cantilever deflection sensor comprised of a laser source and a position sensitive diode (PSD). The scanner, typically a piezoelectric tube, provides three-dimensional motion between the probe and a sample. Information on sample topography or local properties is obtained based on probe-sample interactions. One of the main operating modes of AFM is contact mode. In this mode, the probe presses against a sample, exerting a vertical force proportional to the cantilever deflection. The probe is then dragged against the sample along each scan line in a raster fashion. The slope at the cantilever free-end is measured and fed back. During scanning, a control system is used to maintain a constant slope, by adjusting the vertical displacement of the scanner. Changes in the piezo deflection are therefore, related to changes in the sample topography. This mode is the scope of this paper.

III. Motivation

A commercial AFM was used to scan a Silicon calibration steps. The AFM was run under PI control. A Silicon Nitride cantilever was used with a resonant frequency of 13 kHz and stiffness of 0.2 N/m. Scan results demonstrate the high sensitivity of collected images to scan and controller parameters (K_p and K_i). Comparing Fig. 2 (a) ($72\ \mu m/s$; $K_p = K_i = 2$) to Fig. 2 (b) ($96\ \mu m/s$; $K_p = K_i = 20$), some of the effects of scanning speed and controller gains on the image can be seen. Higher gains result in oscillations as the cantilever falls along the right edge of the step, with peaks probably indicating mo-

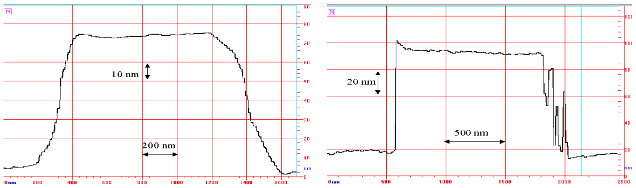

Fig. 2. AFM images: (a) 72 $\mu m/s$; $K_p = K_i = 2$, (b) 96 $\mu m/s$; $K_p = K_i = 20$.

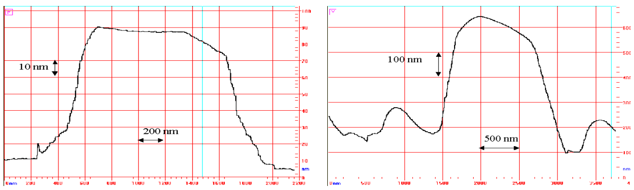

Fig. 3. AFM images: 180 $\mu m/s$, (a) nominal contact force, (b) smaller contact force.

mentary loss of contact between the probe and the sample. While the sharp peak on the left edge of the step, Fig. 2 (b), can be attributed to a high scan speed compared to closed loop bandwidth. The higher gains improve tracking, as the sharp left edge of the step is resolved more accurately. Figures 3 (a) and (b) were generated with a scan speed of 180 $\mu m/s$ using the same controller gains. The contact force set-point for Fig. 3 (a) is set to the manufacturer's recommended value, while Fig. 3 (b) a smaller force was used. Choosing a small contact force set-point reduces contact deformation and friction, however, it reduces stability of the contact. As seen from Fig. 3 (b), the image generated with a small contact force has erroneous height information, due to loss of contact between the probe and the sample.

It has been shown that scan and control parameters dramatically impact AFM dynamics. As a result, image artifact may result because of poor dynamics. In order to eliminate these types of artifacts, we need to understand the dynamic interactions between different components of the AFM. This is the objective of this work.

IV. System Model

We have reported models describing the dynamics of AFM in [4], [5]. It includes probe-sample interaction forces, models for the piezoelectric scanner longitudinal and lateral dynamics and coupling between them, and cantilever flexural dynamics. Sources of noise and disturbances were also discussed. In this section, the models will be briefly presented and discussed.

A. Probe-sample Interaction

A.1 In-contact Model: Vertical Forces

This contact mechanics model [6], is suitable for AFM operation in air or other media where adhesion/capillary forces are dominant. It describes the adhesion/capillary contact of two elastic spheres. A non-dimensional transi-

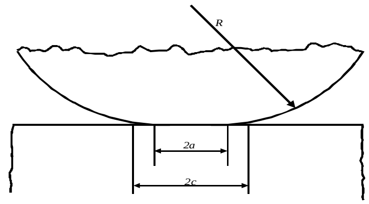

Fig. 4. Schematic of probe-sample contact.

tion parameter λ, was defined as,

$$\lambda = \sigma_0 \left(\frac{9R}{2\pi w E^{*2}}\right)^{\frac{1}{3}} \tag{1}$$

where, σ_0 is the theoretical strength of the adhesion junction, R is the reduced radius of the spheres, w is the Dupré's work of adhesion, and E^* is the combined elastic modulus of the spheres. This transition parameter can be viewed as the ratio of elastic deformation to the effective range over which surface forces act. From (1), it follows that large values for λ would correspond to compliant (small E^*), large spheres (R), and small adhesion (w) contacts, where small values are for stiff small spheres with high adhesion. The model can be used to predict contact force $\bar{F}_{con}$, contact deformation $\bar{\delta}$, and contact radius $\bar{a}$.

The model is composed of three nonlinear algebraic equation that can be expressed in non-dimensional form as,

$$\begin{aligned}
\bar{\delta} &= \bar{a}^2 - \frac{4\lambda\bar{a}}{3}\sqrt{m^2-1} \\
\bar{F}_{con} &= \bar{a}^3 - \lambda\bar{a}^2\left[\sqrt{m^2-1} + m^2\sec^{-1}(m)\right] \\
1 &= \frac{\lambda\bar{a}^2}{2}\left[(m^2-2)\sec^{-1}(m) + \sqrt{m^2-1}\right] + \\
&\quad \frac{4\lambda^2\bar{a}}{3}\left[\sqrt{m^2-1}\sec^{-1}(m) - m + 1\right]
\end{aligned} \tag{2}$$

where, $m = \frac{c}{a}$ as in Fig. 4, c is the radius over which surface forces are present. The use of such continuum models to describe nano-contacts has been supported by many experiments. The level at which continuum models break-down is not all clear [7].

A.2 In-contact Model: Lateral Forces

As the probe is dragged against the sample while in contact, a frictional shear force develops. At nano-level contacts, experiments have revealed the dependence of friction force on contact area, [1]. For our purposes, we are interested in simulating the effect of sliding friction force on the cantilever dynamics during scanning. As a first order approximation, we will assume that the instantaneous friction force is directly proportional to the instantaneous contact area ($\propto a^2$). This model does not consider any explicit dependence of friction on scanning speed. Although contact models were originally developed for static loading, it has been shown in [1], that it holds under sliding conditions with not very high sliding speeds. When the probe and sample are out of contact the friction force is set to zero.

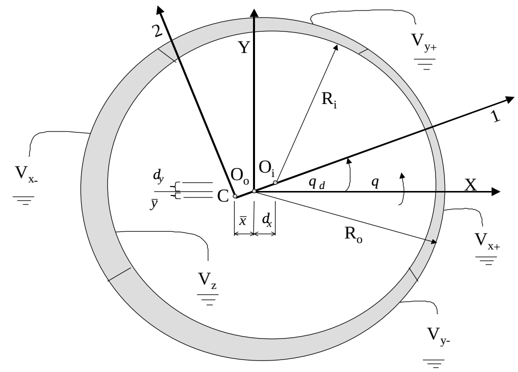

Fig. 5. Cross section of an eccentric piezoelectric tube.

A.3 Out-of-contact Model: Vertical Forces

When the probe and sample are not in contact, van der Waals forces between two spheres are assumed to be the dominant interaction.

A.4 Point of Contact

At the limit of loss of contact, the contact radius $\bar{a} \to 0$. Substituting this into eqn. (2), gives the force and separation at that limit. This is used to impose continuity on the force between models of sections IV-A.1 and IV-A.3.

B. Scanner Lateral Dynamics

There are two main designs for AFM. In one design, the cantilever is fixed and a sample is placed on the scanner which moves it relative to the cantilever. This design, generally, limits the maximum size and weight of the sample. In the second design, Fig. 1, the cantilever is attached to the scanner that moves it relative to a stationary sample. In this paper the model presented is for the second, more popular design.

The scanner is a thin-walled piezoelectric tube that has four electrodes of equal segments on its outer surface, and either a single or four electrode on its inner surface. Applying a voltage V_z, to its inner electrode(s) results in extension motion, (in the Z-axis). Motion in the X or Y axis is typically generated by subjecting two opposite electrodes to two voltage signals, (V_{x_+}, V_{x_-}) and (V_{y_+}, V_{y_-}), with the same magnitude but are out of phase.

In [8], [9], a model for an ideal uncoupled tube scanner was presented. Due to inevitable machining tolerance, eccentricity is always present in the tube. Typically, a maximum of 50 μm for a 12.7mm diameter tube, [10]. This seemingly small eccentricity is in fact significant as the cantilever-deflection sensor has Angstrom rms resolution. The model is based on two eccentric cylinders, Fig. 5, with eccentricity δ_x and δ_y from the geometric center of the outer cylinder, O_o. The tube is fixed at one end and free at the other. A cantilever holder of mass m_{sh} is attached to its free end. The model is based on elementary bending theory for thin-walled members. The main assumptions are small deformations and angles, linear elastic material, and negligible effects of rotary inertia and shear deformation. Below, eqn. (3), gives the transfer function between the input voltages and the lateral displacement u_j; $(j = 1, 2)$, for i^* number of modes. Equations (4), and (5) give the output equations for displacements in the X and Y-directions, x_p and y_p, respectively. The scanner's free end rotations (i.e. slopes) about X and Y-axes, θ_{px} and θ_{py}, respectively, are given in eqn.'s (6) and (7).

$$u_j = \sum_{i=1}^{i^*} \frac{\gamma_{ix_+}V_{x_+} + \gamma_{ix_-}V_{x_-} + \gamma_{iy_+}V_{y_+} + \gamma_{iy_-}V_{y_-} + \gamma_{iz}V_z}{s^2 + 2\zeta_{iu_j}\omega_{iu_j}s + \omega_{iu_j}^2} \tag{3}$$

$$x_p = \cos(\theta_\delta)\, u_1 - \sin(\theta_\delta)\, u_2 \tag{4}$$

$$y_p = \sin(\theta_\delta)\, u_1 + \cos(\theta_\delta)\, u_2 \tag{5}$$

$$\theta_{px} = \sin(\theta_\delta)\frac{\partial u_1}{\partial z} + \cos(\theta_\delta)\frac{\partial u_2}{\partial z} \tag{6}$$

$$\theta_{py} = \cos(\theta_\delta)\frac{\partial u_1}{\partial z} - \sin(\theta_\delta)\frac{\partial u_2}{\partial z} \tag{7}$$

C. Scanner Longitudinal Dynamics

The details of the model are given in [11]. The main assumptions are similar to those of section IV-B. The transfer function between input voltages and displacement of the tube's free-end z_p, for j^* number of modes is given as,

$$z_p = \sum_{j=1}^{j^*} \frac{\gamma_{jx_+}V_{x_+} + \gamma_{jx_-}V_{x_-} + \gamma_{jy_+}V_{y_+} + \gamma_{jy_-}V_{y_-} + \gamma_{jz}V_z}{s^2 + 2\zeta_{jz_p}\omega_{jz_p}s + \omega_{jz_p}^2} \tag{8}$$

D. Scanner Creep

The response of a piezoelectric actuator to a rapid change in input voltage, Fig. 6, consists of two main parts. The initial part of the response occurs over a time scale dictated by the mechanical resonance of the actuator. This is followed by a slow creeping response occuring over 10's of seconds and amounting to as much as 20% of the total response. The rate and amount of creep strongly depend on the piezoelectric material. Experimental frequency response of piezoelectric actuators displays very little variation in phase at low frequency between input voltage and displacement. On the other hand, a slight decrease in gain is observed with increasing frequency. It is possible to simulate creep behavior using a suitable LTI model. The relative degree is number of poles minus the number of zeros of the transfer function. The transfer function between the input voltage and actuator displacement should have a relative degree zero at frequencies much lower than the actuator's resonance frequency. This model assumes that the ratio between the amount of creep and the fast scanner displacement is independent of input amplitude. The assumption will be experimentally tested.

E. Cantilever Flexural Dynamics

This dynamic model for the cantilever motion neglects effects of shear deformation and rotary inertia, and is based

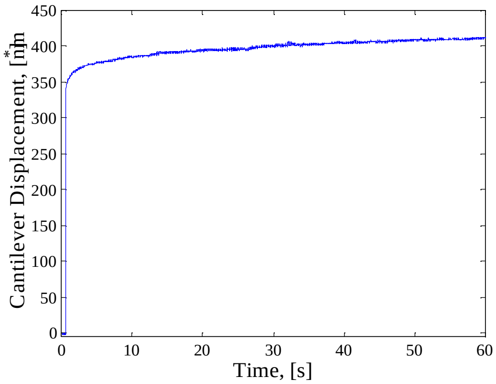

Fig. 6. Experimental creep response.

on elementary bending theory. The cantilever slope (angle), z_c^0, is measured relative to its base motion, $z_p(t)$. The boundary conditions are taken as zero deflection and slope relative to the base at the fixed end, and zero moment and shear force at the free-end. For simplicity, the cantilever is assumed to be aligned with the X-axis. The transfer function governing the cantilever's response is given by,

$$
\begin{aligned}
z_c^0(s) \;=\; & \sum_{m=1}^{\infty} \frac{a_{2zm}\, s^2 + a_{1zm}\, s}{s^2 + 2\zeta_{cm}\,\omega_{cm}\, s + \omega_{cm}^2}\, z_p(s) \\
& + \frac{a_{2\theta m}\, s^2 + a_{1\theta m}\, s}{s^2 + 2\zeta_{cm}\,\omega_{cm}\, s + \omega_{cm}^2}\, \theta_{py}(s) \\
& + \frac{a_{fm}}{s^2 + 2\zeta_{cm}\,\omega_{cm}\, s + \omega_{cm}^2}\, f(z_c; z_p; \theta_{py}; z_s) \quad (9)
\end{aligned}
$$

where, $f(z_c; z_p; \theta_{py}; z_s)$ is the probe-sample force, and z_s is the sample height.

F. Sensor Output

The optical-lever sensor measures the absolute angle of the cantilever's free-end. Therefore, the PSD output y_{PSD}, is given by,

$$
y_{PSD} \;=\; \theta_{py} - z_c^0 \qquad (10)
$$

G. Disturbances

Thermal noise or Brownian motion contributes to a fundamental source of noise in AFM. At thermal equilibrium, the mean value of the cantilever potential energy has to equal $\frac{1}{2}k_B T$, where $k_B = 1.38 \times 10^{-23}$ J/K is Boltzmann's constant, and T is the absolute temperature in Kelvin. The cantilever's free-end will oscillate with a RMS value, $z_c^{0\,rms} = \frac{3}{2L_c} z_c^{rms} = \frac{3}{2L_c}\sqrt{\frac{k_B T}{k_c}}$, where k_c is the cantilever stiffness, and L_c is the cantilever length. This expression is valid for a free standing cantilever. If the cantilever is in contact with a sample, the expression has to be modified by including the sample effective stiffness in k_c. Another source of disturbance is laser back-action. It is due to incidence of photon flux from the optical sensor on the cantilever. Both thermal and back-action noises will be effectively modeled as zero-mean white noise force disturbances with a combined constant intensity $\theta\delta(t - \tau)$.

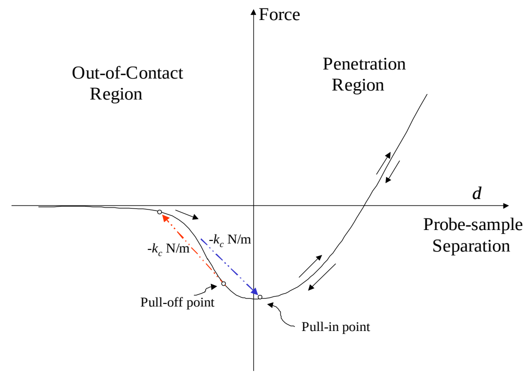

Fig. 7. Simulation: Quasi-static normalized force-separation curve.

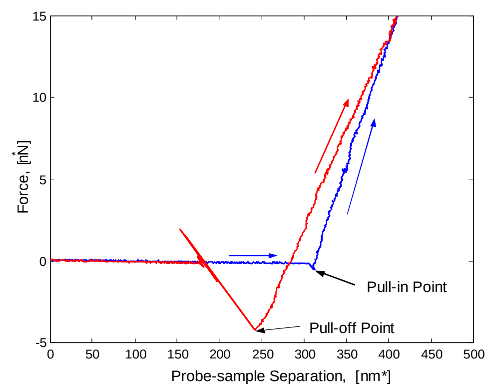

Fig. 8. Experimental force-displacement curve.

Feedback measurement noise arising from the optical sensor can be due to shot noise, a fundamental noise for these sensors, in addition to noise from sensor electronics. Shot noise can also be modeled as white noise.

V. Results

A. Quasi-static Force-separation Curve

The models of sections IV-A.1, IV-A.3 were used to generate the composite force-separation curve of Fig. 7. Parameters used to generate the curve are given in [4]. It is worth noting that eqn. (2) can predict an instability that has been observed in quasi-static experiments. This instability occurs when an approaching/receding probe jumps in/out (pull-in/pull-out points), of contact with the sample surface corresponding to a sudden jump in the contact area. The actual point of instability on the force-separation curve will depend on the stiffness of the cantilever k_c, as shown in Fig. 7. An experimental force-separation curve is shown in Fig. 8, where * denotes use of estimated calibration factors. It shows the same characteristic produced by the model in Fig. 7, except that hysteresis is observed in the penetration region as the approach and retract lines are not the same.

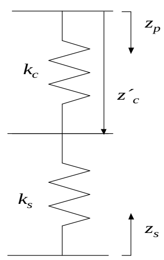

Fig. 9. Schematic of probe-sample contact.

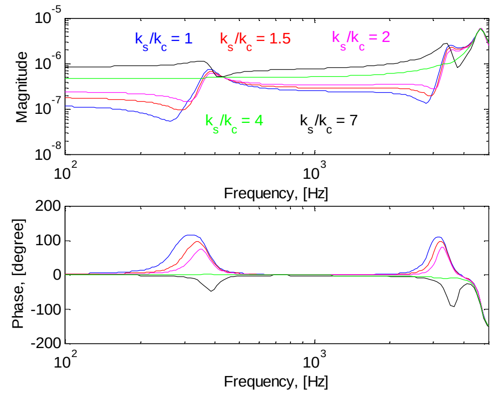

Fig. 10. Simulation: In-contact frequency response for different ratios of sample to cantilever stiffness $\frac{k_s}{k_c}$.

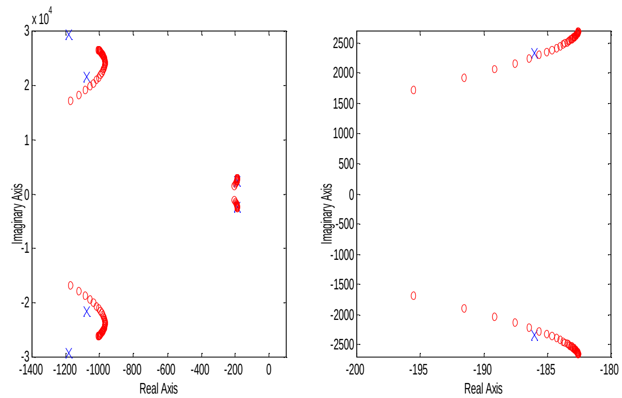

Fig. 11. Pole-zero map as a function of $\frac{k_s}{k_c}$: (left) zoom on 2kHz mode, (right) zoom on 380Hz mode.

B. In-contact Dynamics: Simulations

The probe-sample interaction force $f(z_c; z_p; \mu_{py}; z_s)$ is a nonlinear function of probe-sample separation, and depends on geometry, environment, and probe and sample material properties. To obtain a linear model to be used for analysis, the force was expanded in a Taylor series and linear terms were retained, giving,

$$\begin{aligned} f(z_c; z_p; \mu_{py}; z_s) &= g_c z_c + g_z z_p + g_{\mu_{py}} \mu_{py} \\ &\quad + k_s z_s + H.O.T. \end{aligned} \qquad (11)$$

k_s can be considered as a linear effective probe-sample contact stiffness. The probe-sample contact can be represented schematically as in Fig. 9, where again z_c, is measured relative to z_p. The contact and cantilever stiffness k_c, are represented as two springs in series. The contact stiffness does not change the order of the model, but has a great impact on the system's zeros. Substituting eqn.'s. (3), (7), (8), and (11) into eqn. (9) and the resulting equation into eqn. (10) gives the overall model. The transfer function of interest is between V_z and y_{PSD}. This describes the AFM Z-dynamics, which we will focus on in this work.

The model used in this study included four bending modes and two extension modes for the scanner, and one bending mode for the cantilever. The parameter values used are given in [11]. The ratio of sample to cantilever stiffness $\frac{k_s}{k_c}$, proved to be an important parameter. Changes in this ratio have two main effects on the model, namely, change in the transfer function DC gain and changes in the frequency of the zeros associated with the scanner bending modes, 380Hz and 2kHz. Figure 10, shows the simulated frequency response of the model for different ratios of stiffnesses. For large ratios (e.g. $\frac{k_s}{k_c} = 7$), the zeros have a higher frequency than the mode. For smaller ratios (e.g. $1 \le \frac{k_s}{k_c} \le 2$), the frequency decreases to be below that of the mode. This change in pole-zero pattern is referred to as pole-zero flipping. Moreover, for some value ($\frac{k_s}{k_c} \approx 4$), there is pole-zero cancelation and the bending modes are unobservable. Figure 11, presents a pole-zero map of the first two modes for different values of $\frac{k_s}{k_c}$. As a result, as the zeros move away from the mode, the resonance peak appears more prominent in the response. Further, when $\frac{k_s}{k_c}$ is either too large or too small, the DC gain reaches a limit controlled by k_c and k_s, respectively. For intermediate values, the DC gain will depend on both stiffnesses and changes in k_s due to different set-pints or input amplitudes will change the DC gain, and zeros location.

C. In-contact Dynamics: Experiments

To investigate in-contact AFM dynamics and validate the models, two samples were chosen for experiments, namely, a Glass and a Polydimethylsiloxane (PDMS), sample having Young's moduli of elasticity of 60 and 25MPa, respectively. Two different cantilevers were used. Cantilever A has an estimated stiffness of 0.03N/m and resonance frequency of 13kHz. Cantilever B has an estimated stiffness of 0.14N/m and resonance frequency of 14kHz. Different set-points and input amplitudes were used to study the effect of these parameters on the dynamics.

Figure 12, shows the force-displacement curve for the Glass sample. The points labeled on the plot are the force set-points used in the frequency response experiments. Note that the local sensitivity around the set-points (cantilever deflection per scanner input voltage) is smaller for the larger force set-point. This suggests reduced contact stiffness potentially due to plastic deformation in the contact. The effects of force set-point on the dynamics are seen in Fig. 13. For the larger set-point, 17nN, the DC

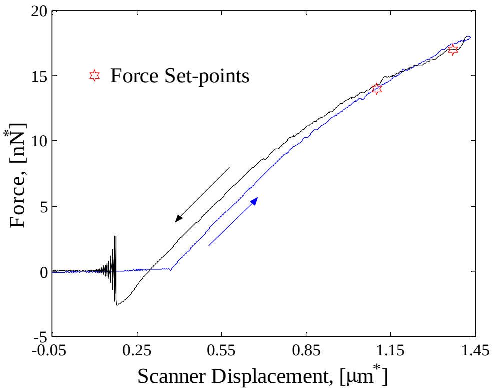

Fig. 12. Force-displacement curve using cantilever A with a Glass sample.

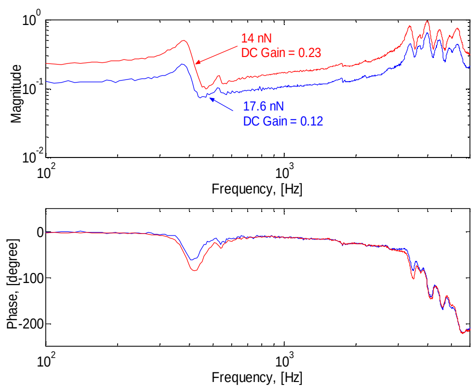

Fig. 13. In-contact frequency response using cantilever A with a Glass sample: same amplitude for different set-points.

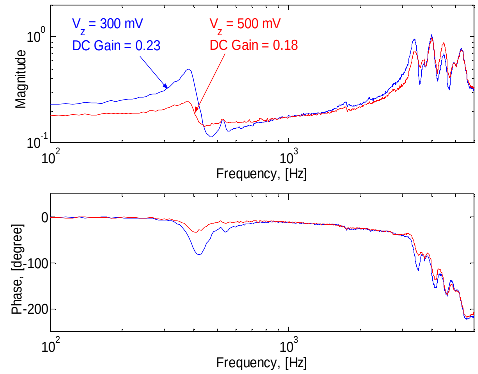

Fig. 14. In-contact frequency response using cantilever A with a Glass sample: 14nN for different amplitudes.

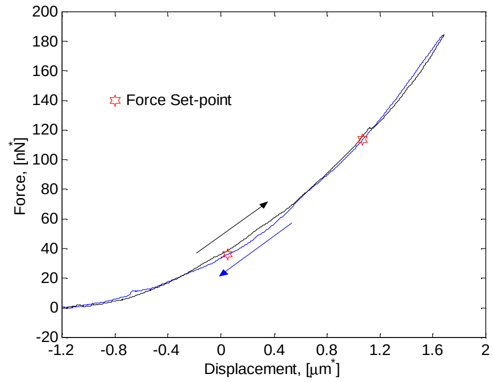

Fig. 15. Force-displacement curve using cantilever B with a PDMS sample.

gain is smaller and the 380Hz bending mode has a smaller resonance peak. The decrease in DC gain suggest that the effective contact stiffness has decreased, hence, the scanner displacement (Fig. 9) is transmitted more to the smaller stiffness; the contact's. The smaller resonance peak could be due to two reasons; the frequency of the zero-pair associated with the bending mode has slightly decreased for the larger set-point. Hence, allowing the contribution of the bending mode to appear less prominent in the response. In addition, it could be a result of changes in the dissipative properties of the contact with changes in the set-point. It is important to realize that the bending mode resonance frequency did not change. The contact forces are orders of magnitude smaller than the force the scanner can provide, ($\approx 10^{-9}$nN vs. ≈ 1N).

The effect of excitation amplitude, i.e. sample topography, on the frequency response is shown in Fig. 14, for set-point of 14nN. It is seen that the larger the amplitude of excitation, the smaller the DC gain. For the larger input amplitude, more plastic deformation might occur in the contact due to the larger contact force, which in turn reduces the effective contact stiffness. As before, more displacement is transmitted to the sample, hence, reducing the DC gain. The more plastic deformation there is, the smaller the change in contact stiffness, and hence DC gain. The resonance peak also changes due to changes in the frequency of the bending mode zero-pair.

Figure 15, shows the force-displacement curve for the PDMS sample. The penetration region seems quite nonlinear. This implies that what is being measured by the PSD signal, at least in part, is the deformation of the sample. The observations in Fig. 16, are that increasing the input amplitude reduces the DC gain, the frequency of bending-mode zeros, and consequently increasing resonance peak. This suggests that the contact stiffness increases with larger amplitude, which agrees with Fig. 15. In addition, increasing set-point, Fig. 17, results in pole-zero flipping for the first two bending modes. The frequency of the zeros changes from being higher to being lower than that of the associated mode. This is in agreement with model predications in section V-B, (Fig. 10). Hence, contact and cantilever stiffness values are relatively close.

The model can be further improved on to include nonlinearities in the contact affecting the DC gain and damping. These nonlinearities depend in great part on properties of the sample. Hence, the form of this dependence is not known. It is possible to account for it in the model by generalizing the probe-sample force to include dissipative terms and retain higher order terms. Therefore, eqn. (11), changes to $f(z_c, \dot{z}_c, z_p, \dot{z}_p, \mu_p y, \mu_{\dot{p}} y, z_s)$.

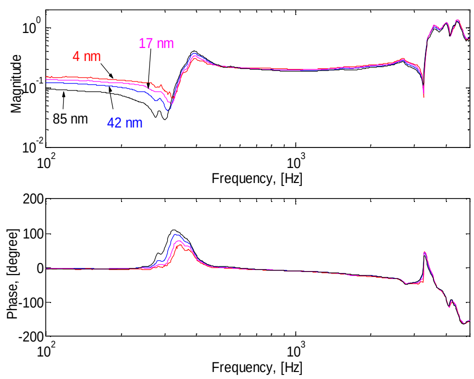

Fig. 16. In-contact frequency response using cantilever B with a PDMS sample: 36 nN for different amplitudes.

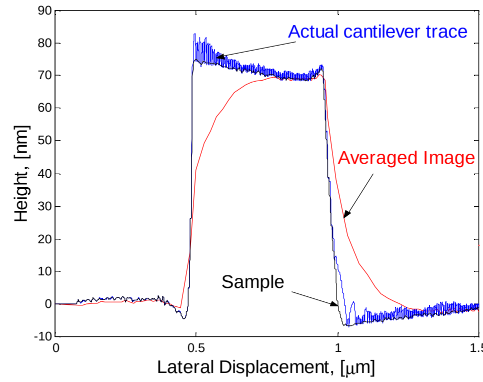

Fig. 18. Scanning simulation results of calibration steps using a PI controller.

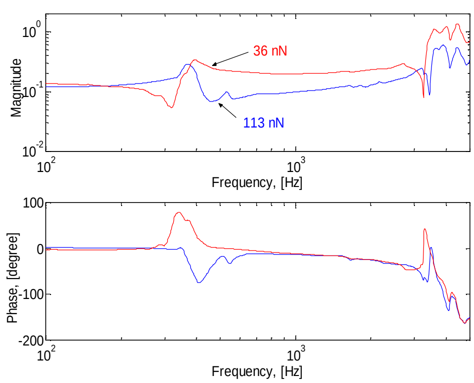

Fig. 17. In-contact frequency response using cantilever B with a PDMS sample: 17 nm amplitude for different set-points.

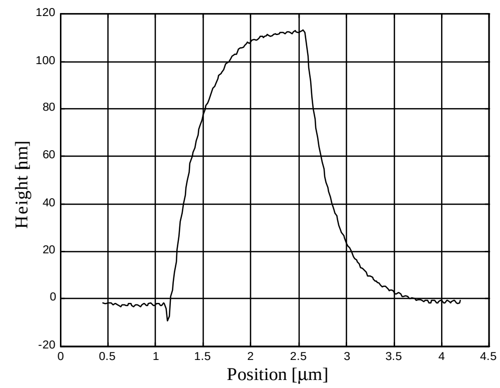

Fig. 19. AFM image of calibration steps using a PI controller.

D. Scanning Simulation vs. Experiments

The models were used to perform scanning simulations. The sample shape used in simulation is an experimental AFM image of calibration steps. Figure 18, shows the simulated image vs. the actual sample. It can be seen that the sampled and averaged image generated from the piezo voltage, V_z, does not correspond well to the actual image. The cantilever oscillations causes it to loose contact with the sample and the hammering action could in fact be damaging to the actual sample. AFM image shown in Fig. 19 is of the steps used in the simulation. The simulations predict the actual response well. Also note the oscillations observed in Fig. 19. These oscillations introduces an artifact that could be interpreted incorrectly as surface roughness.

E. Performance Limitations Due to Scanner Bending Mode

The coupling between scanner bending and extension modes has a great impact on AFM performance in several ways. When the scanner is commanded to move up/down, there is a slight bending motion that gets detected by the PSD. The scanner is typically calibrated by imaging a standard of known height usually in the 100nm range. During imaging, the PSD signal will change due to the sample topography as well as to bending of the actuator. Imaging a sample of a different height will result in a slightly different calibration factor, even if the nonlinearity of the scanner was not a concern. The change in calibration due to scanner bending is typically less than 1%.

Scanner extension mode is typically around 4 to 8 kHz. The required feedback bandwidth during scanning can be estimated based on scan rate and image resolution (number of data points per scan line). For a scan rate of 2 Hz and a resolution of 512, the bandwidth would be $2 \times 2 \times 512/1000 = 2.048$ kHz. Hence, the bending resonance at 380 Hz would be well within the feedback bandwidth. Tuning the controller gains to achieve a high bandwidth would result in oscillations in the image. This can be seen in Fig. 20, where oscillations due to the 380 Hz mode is observed in an experimental AFM image. Increasing force set-point tends to make the bending mode less observable by moving the zeros closer to that poles. However, the high contact force may cause damage to the sample and/or reduce image resolution. Alternatively, the bandwidth can be reduced along with scan speed. This results in a longer scan time making scanner creep more observable in the image. Further, since the bending mode is the closest mode to the $j\omega$ axis, Fig. 11, it has a great effect on the robustness of the feedback system. Pole-zero flipping can cause closed loop poles to cross the $j\omega$ axis causing feedback instability.

F. Creep Compensation

A 3rd order LTI filter was used to compensate for creep in the AFM piezoelectric scanner, [12]. The performance

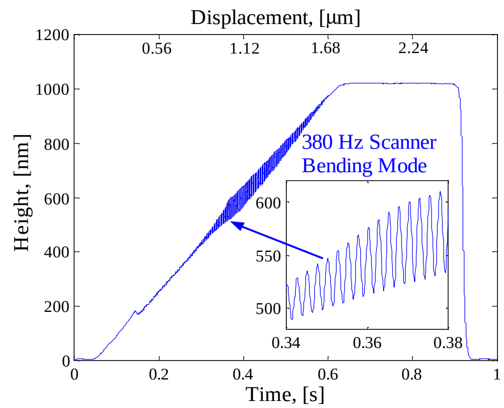

Fig. 20. Oscillations due to scanner bending mode in experimental AFM image of a 1046 nm Silicon step.

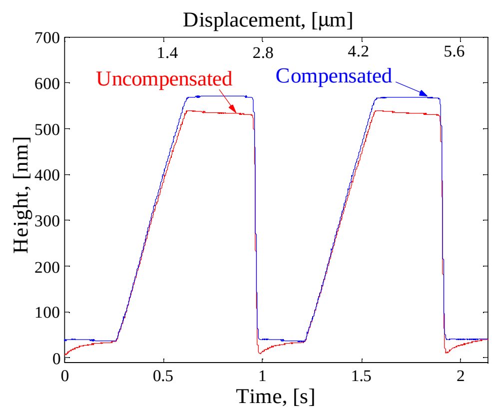

Fig. 21. AFM image of 530nm Silicon steps, with and without creep compensation, 28 μm/s.

of the filter was tested, e.g. Fig. 21, by imaging 530 and 1590nm steps. With compensation, the creep response was reduced to 26% with compensation for images taken over 667 minutes. Compensation did not degrade for larger steps, suggesting that a linear model for creep may be justified. Nonlinearities in the scanner fast displacement can be dealt with separately. Closed loop operation can offer better creep compensation but is a more expensive option. In addition, it reduces image resolution for small scans/sample features due to limited dynamic range of the sensors at a high bandwidth.

VI. Summary and Conclusion

The quality of AFM data strongly depends on scan and controller parameters. Data artifacts can result from poor dynamic response of the instrument. In order to achieve reliable data, dynamic interactions between AFM components need to be well understood and controlled. In this paper we presented a summary of our work in this direction. It included models for the probe-sample interaction, scanner lateral and longitudinal dynamics, scanner creep, and cantilever dynamics. The models were used to study the effect of scan parameters on the system dynamics. Simulation results for both frequency response and imaging were presented. Experimental results were given supporting the simulations and demonstrating the competence of the models. The results within will be used to develop algorithms that allow automated choice of key system parameters, guaranteeing reliable and artifact-free data for any given operating condition (sample, cantilever, environment). Consequently, expanding the AFM capabilities and permitting its use in a wider range of applications.

References

[1] A. M. Homola, J. N. Israelachvili, M. L. Gee, and P. M. McGuiggan, Measurements of and Relation Between the Adhesion and Friction of 2 Surfaces Separated by Molecularly Thin Liquid-Films, Journal of Tribology, Vol. 111 (4), pp. 675-682, 1989.

[2] El Rifai, O. M., and Youcef-Toumi, K., On Factors Affecting The Performance of Atomic Force Microscopes in Contact-mode, 1999 IEEE/ASME International Conference on Advanced Intelligent Mechatronics, Atlanta, GA, USA, 19-23 September, 1999, pp. 21-26.

[3] N. A. Burnham, O. P. Behrend, F. Oulevey, G. Gremaud, P-J Gallo, D. Gourdon, E. Dupas, A. J. Kulik, H. M. Pollock, and G. A. Briggs, How Does a Tip Tap, Nanotechnology, Vol. 8, pp. 67-75, 1997.

[4] El Rifai, O. M., and Youcef-Toumi, K., Dynamics of Contact-mode Atomic Force Microscopes, American Control Conference, Chicago, Illinois, USA, June 28-30, 2000.

[5] El Rifai, Osamah M., and Youcef-Toumi, Kamal, Coupling in Piezoelectric Tube Scanners Used in Scanning Probe Microscopes, American Control Conference, Arlington, Virginia, USA, June 25-27, 2001.

[6] D. Maugis, Adhesion of Spheres: The JKR-DMT Transition Using a Dugdale Model, Journal of Colloid and Interface Science, Vol. 150 (1), pp. 243-269, 1992.

[7] K. L. Johnson, Continuum Mechanics Modeling of Adhesion and Friction, Langmuir, Vol. 12, pp. 4510-4513, 1996.

[8] Tetsuo Ohara, and K. Youcef-Toumi, Dynamics and Control of Piezotube Actuators for Subnanometer Precision Applications, Proceedings of the American Control Conference, Seattle, Washington, pp. 3808-3812, June 1995.

[9] Taylor M. E., Dynamics of Piezoelectric Tube Scanners for Scanning Probe Microscopy, Review of Scientific Instruments Vol. 64 (1), pp. 154-158, January 1993.

[10] Stavely Sensors Inc., EBL Product Line Catalog, 91 Prestige Park Circle, East Hartford, CT 06108-1918.

[11] Osamah El Rifai, and Kamal Youcef-Toumi, Modeling of Atomic Force Microscope Dynamics, to appear

[12] El Rifai, Osamah M., and Youcef-Toumi, Kamal, Creep in Piezoelectric Scanners of Atomic Force Microscopes, to appear